Letter

Geometry-dependent topological ultrasound cavities in valley sonic crystals

Lang Nie,[1,2,*] Yi Fang,[3,*] Qing Wang,[3] Jien Wu,[2] Hailong He,[3,†] Zhaojian He,[2,‡] Ke Deng,[2,§] Jiuyang Lu,[3] Manzhu Ke,[3] and Zhengyou Liu[3,4]

[1]*Department of Physics, Jishou University, Jishou 416000, Hunan, China*
[2]*School of Physics and Electronic Science, Changsha University of Science and Technology, Changsha 410114, Hunan, China*
[3]*Key Laboratory of Artificial Micro- and Nano-Structures of Ministry of Education and School of Physics and Technology, Wuhan University, Wuhan 430072, China*
[4]*Institute for Advanced Studies, Wuhan University, Wuhan 430072, China*

(Received 26 August 2025; revised 4 May 2026; accepted 13 May 2026; published 1 June 2026)

Topological edge states, immune to backscattering, present challenges in confining them to specific positions within a waveguide. Topological photonic cavities have been shown to localize edge states along their propagation path, opening unique opportunities for manipulating and collecting electromagnetic waves. In this Letter, we realize a geometry-dependent underwater topological ultrasound cavity, created using a valley sonic crystal waveguide terminated by a rigid reflector. The strong confinement of sound wave energy in the oblique reflector surface is experimentally observed through ultrasound frequency- and time-domain measurements, which is due to the extended time delay of the valley polarization flipping. We further demonstrate that the valley-flipping time at the reflector surface is dependent on the edge configuration of the valley sonic crystals and the orientation of the reflector. Our Letter introduces a strategy for designing topological acoustic cavities and achieving ultrasonic wave confinement in underwater environments.

DOI: 10.1103/hf4m-sql4

Topological edge states, a defining feature of topological phases of matter, have attracted considerable attention due to their robustness against backscattering, rendering them resilient to disorder and imperfections in waveguides [1–9]. This intrinsic stability, however, poses significant challenges when attempting to localize these edge states within specific regions of a waveguide [10–13]. Notably, valley-protected edge states, characterized by nonzero valley Chern numbers, exhibit remarkable resistance to flipping their valley-locked momentum under weak disorder [14–20]. Recently, various artificial topological cavities [21–29], created by introducing point or line defects in topological systems, have been proposed as a means to trap, delay, or redirect electromagnetic or acoustic waves, opening avenues for novel applications in topological lasers [30–33], integrated optics [34,35], robust delay lines [36,37], and quantum information processing [38]. More recently, a topological photonic cavity created by straightforwardly terminating the photonic crystal waveguide with a terminal mirror has successfully demonstrated the ability to halt valley-polarized edge states [39,40].

Thanks to the design and fabrication flexibility of sonic crystals (SCs), nonzero valley Chern numbers can easily be achieved by rotating the triangular scatterers to break inversion symmetry [41,42], leading to the observation of hallmark valley-polarized edge states in acoustic systems [17,19,43]. Recent advancements have also introduced boundary-induced chiral anomaly bulk states in sonic metamaterials within airborne or elastic wave media, where the group velocity direction can be reversed through boundary adjustments, presenting a novel approach for developing valley-based sonic devices [44–46]. However, despite the significant impact of the surrounding water medium on acoustic mode conversion, research in underwater topological acoustics remains scarce. Waterborne SCs, with their macroscopic scale, provide an ideal platform for exploring these unique interactions, offering promising potential for breakthroughs in applications such as underwater invisibility cloaking [47], acoustic communication [48], and acoustic tweezers [49].

In this Letter, we present the realization of a geometry-dependent underwater topological ultrasound cavity formed by a valley SC (VSC) waveguide terminated by a rigid reflector. The design leverages the unique features of VSCs to manipulate the propagation of sound waves, specifically by confining energy along the surface of the reflector. This strong confinement of sound wave energy is experimentally demonstrated using both frequency- and time-domain ultrasound measurements. The underlying mechanism for this confinement is attributed to the extended time delay caused by the flipping of valley polarization as the sound waves interact with the reflector. The edge configuration of the VSCs and the oblique angle at which the reflector is positioned significantly affect the duration of the valley flipping, highlighting the potential for fine-tuning the design of topological acoustic cavities. The ability to control and direct these sound waves opens new avenues for applications in underwater acoustics,

*These authors contributed equally to this work.
†Contact author: hehailong@whu.edu.cn
‡Contact author: hezj@whu.edu.cn
§Contact author: dengke@csust.edu.cn

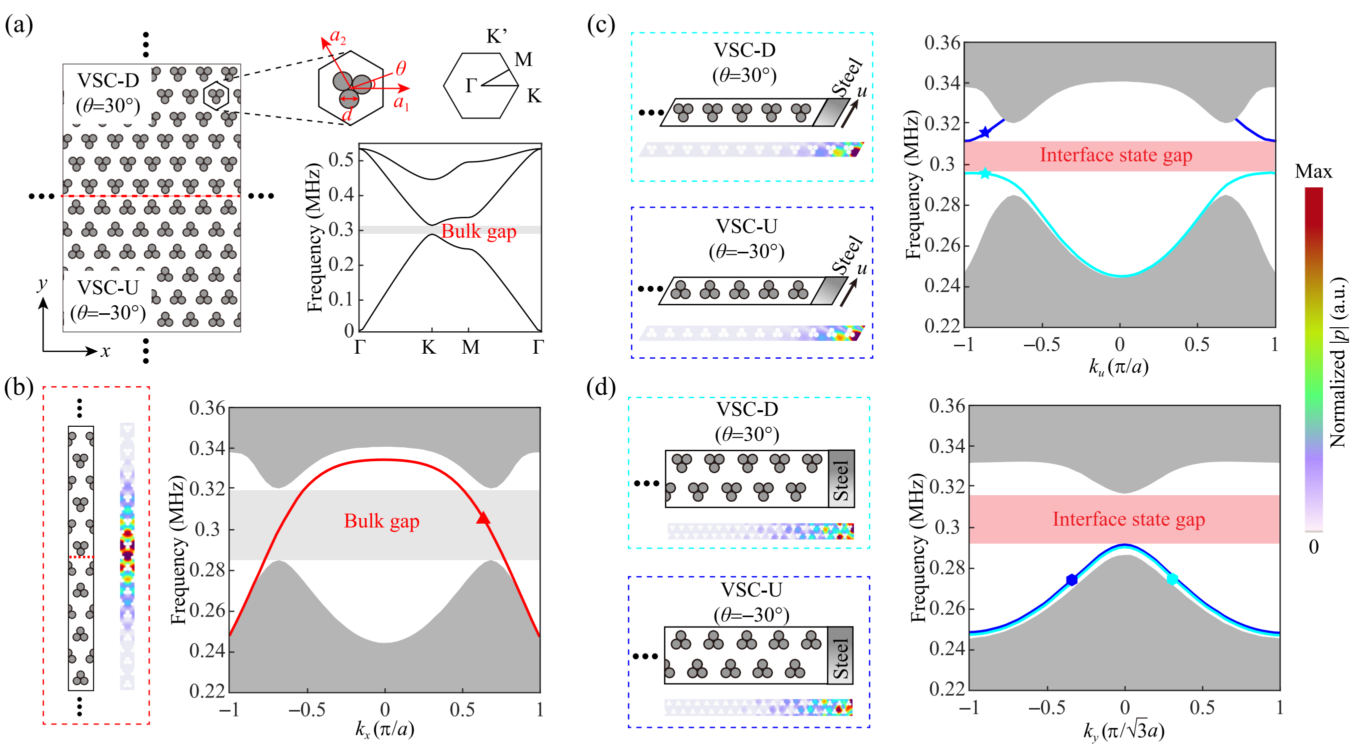

FIG. 1. (a) Left panel: The VSC waveguide made of a triangular lattice of meta-molecules consisting of three closely packed steel cylinders. The red dashed line marks the interface between the upper VSC-D and lower VSC-U. Right panel: The first Brillouin zone of the VSCs and the bulk band structure for the orientation angle $\theta = 30^\circ$. (b) Left panel: The supercell of the waveguide formed by the VSC-D and VSC-U, and the corresponding eigenfield distribution of valley edge states at $k_x = 0.60\pi/a$. Right panel: The projected band dispersion of the supercell in the left panel. Red line denotes the valley-polarized edge state, while gray shadows represent the projected bulk bands. (c) Supercells of the VSCs with the oblique steel reflector, along with their corresponding projected band dispersions. Insets display the eigenfields of the interface states. (d) Supercells of the VSCs with the vertical steel reflector, along with their corresponding projected band dispersions.

particularly in the areas of ultrasonic detection, localization, and waveguide-based signal transmission.

The underwater VSC consists of trimers arranged in triangular arrays, as schematically shown in the left panel of Fig. 1(a). These trimers are constructed from three tightly bound steel cylinders, each with a diameter of $d = 0.8$ mm. The lattice constant of VSC is $a = 2.8$ mm, and the orientation angle θ of the trimer relative to the x axis is shown in the inset of Fig. 1(a). The material properties are as follows: the sound velocity and mass density of water are $c_w = 1500$ m/s and $\rho_w = 1000$ kg/m^3, respectively; while for steel, the bulk modulus, shear modulus, and mass density are 1.682×10^{11} Pa, 7.98×10^{10} Pa, and $\rho_s = 7800$ kg/m^3, respectively. The bulk band structure of the system for an orientation angle of $\theta = 30^\circ$ is shown in the right panel of Fig. 1(a), where a full bandgap is observed, spanning frequencies from 0.287 to 0.317 MHz. We denote the trimers with $\theta = 30^\circ$ and -30° as VSC-D and VSC-U, which exhibit opposite valley Chern numbers. Consequently, a valley-polarized edge state appears within the projected bandgap of the ribbon that connects VSC-D and VSC-U, as illustrated in Fig. 1(b). As we can see from the eigenfield of the edge state, the sound field is primarily confined within the interface.

We now focus on the interface between the VSCs and a rigid reflector with an oblique angle. The projected band structures for the interfaces between VSCs (VSC-D or VSC-U) and a rigid reflector with an oblique angle of 60° are shown in the right panel of Fig. 1(c). As seen, the interface state (cyan line) for the VSC-D/rigid reflector lies at the lower edge of the bandgap, while the interface state (blue line) for the VSC-U/rigid reflector is positioned at the upper edge of the bandgap. The corresponding eigenfields of these interface states are displayed in the same panel. Notably, an interface state gap highlighted in red appears within the projected bulk bandgap of the VSCs. For the vertical reflector, the dispersions of the interface states for the VSC-D/rigid reflector (cyan line) and VSC-U/rigid reflector (blue line) overlap, as shown in Fig. 1(d). Again, an interface state gap emerges within the bulk bandgap of the VSCs, and the eigenfields for these interface states are also provided.

To realize an underwater topological ultrasound cavity, we terminate the VSC waveguide with a rigid reflector, as schematically shown in Fig. 2(a). A sufficiently thick steel reflector is placed at the termination of the interface between VSC-D and VSC-U. The valley-polarized edge states propagate along the VSC interface and encounter the rigid reflector. There are three possible pathways for the ultrasound waves: (1) the waves may be reflected by the rigid reflector after a valley flip (from K to K'); (2) the waves may propagate upward along the interface between VSC-D and the oblique reflector; and (3) the waves may propagate downward along the interface between VSC-U and the oblique reflector.

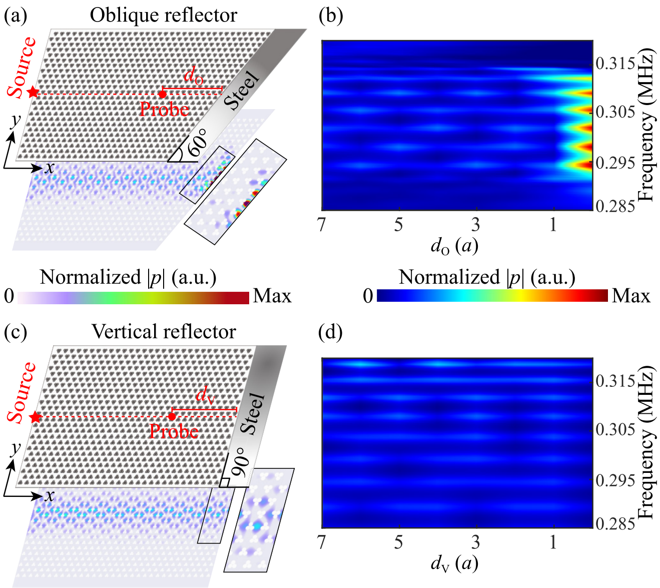

FIG. 2. (a) Upper panel: Schematic of the topological ultrasound cavities formed by the VSC waveguide terminated by an oblique reflector. The sufficiently thick steel with tilt angle 60° is treated as rigid boundary. The red star and dot represent the position of the source and probe, respectively. Lower panel: Sound field distributions of the topological cavities excited by the point source from the left side of the sample at a frequency $f = 0.3$ MHz. (b) Sound field distributions along the interface outlined by the dashed line in (a), varying with frequency. d_o denotes the distance between the probe and reflector. (c, d) Same as (a) and (b), but for the topological cavities terminated by a vertical steel reflector with tilt angle 90°.

However, the valley-polarized edge states within the interface state gap, upon encountering the mirror termination, cannot propagate through the upward or downward interfaces. As a result, the edge states are reflected to the VSC interface, requiring the valley index of the topological edge states to flip from K to K'. The rate of valley-index flipping is equivalent to the leakage rate of the topology-controlled photonic cavity [39,40].

When a Gaussian ultrasound wave packet is incident on the sample from the left boundary, with a frequency within the interface state gap, the wave excites the K-valley polarized edge state, which propagates along the VSC interface before encountering the rigid reflector. Upon reflection, the valley-polarized edge state undergoes a valley flip from the K valley to the K' valley after some time. This results in the formation of a topological ultrasound cavity at the intersection of the VSC interface and the VSC/reflector interface. In the lower panel of Fig. 2(a), we present simulated field distributions for ultrasound waves with a frequency of $f = 0.3$ MHz. The sound fields are predominantly confined along the waveguide, with a significant increase in sound intensity at the intersection, thereby forming a well-localized cavity. In contrast, for the vertical reflector in Fig. 2(c), the sound fields are nearly evenly distributed along the VSC interface at $f = 0.3$ MHz, indicating the absence of a distinct cavity at the vertical reflector interface. The corresponding eigenfields for the two types of reflectors can be found in the Supplemental Material [50].

To further elucidate the differences of sound intensities between the ultrasound cavities, we plot the field intensity as a function of frequency f (ranging from 0.285 to 0.32 MHz) and the distance $d_{O(V)}$ (from the intersection point) in Figs. 2(b) and 2(d), respectively. For the oblique reflector, the sound intensity exhibits a peak rise at the intersection point, rapidly diminishing with increasing distance and eventually leveling off at larger distances, thereby confirming the formation of a well-defined ultrasound topological cavity. In contrast, for the vertical reflector, there is no distinct peak at the intersection; although the field intensity is slightly enhanced at this location compared to other points, it is insufficient to establish a clear cavity. These results indicate that the rate of valley-index flipping is strongly dependent on the termination configuration of the topological cavities. The oblique reflector termination (rigid reflector surface with an oblique angle of 60°) effectively suppresses intervalley scattering due to valley conservation, whereas the vertical reflector termination (rigid reflector surface with a right angle of 90°) results in a significantly higher valley-index-flipping rate, as it breaks valley conservation [39,40,51].

We then implement topological ultrasound cavities to measure the valley-index-flipping time. The experimental configurations of the ultrasound cavities with oblique and vertical reflectors are shown in Figs. 3(a) and 3(e), respectively. Two perforated plastic plates are used to precisely align the steel scatterers, with multiple detection points drilled along the waveguide to measure the acoustic response at distances $d_{O(V)}$. A Gaussian pulse, generated by an ultrasonic transducer with a diameter of 25 mm, is incident on the sample from the left boundary. To measure the incident and reflected wave responses at various positions, a needle pinducer with a diameter of 1.9 mm is inserted along the waveguide, as indicated by the red dots. In Figs. 3(b) and 3(f), we present the sound pressure at $d_{O(V)} = 17a$ as a function of time at $f = 0.3$ MHz, for the oblique and vertical reflector samples, respectively. The shaded regions represent the time difference between the first incident and reflected peaks, which corresponds to the transmission time of the edge state along the waveguide, as well as the valley-flipping time from the K valley to the K' valley. This time difference can be expressed as $T_{d_{O(V)}} = \frac{2d_{O(V)}}{V_g} + t_f$, where V_g is the group velocity of the edge states, and t_f is the delay time required for the valley flipping. The time differences observed are $T_{d_O} = 161$ μs (for the oblique reflector) and $T_{d_V} = 104$ μs (for the vertical reflector), resulting in a 57-μs difference between the two samples, which validates our previous analysis. For comparison, we also perform the simulation calculation on the samples. The detailed simulation results can be found in the Supplemental Material [50]. It demonstrates that the flipping time for the sample with an oblique reflector is about 62 μs, while the flipping time for the sample with a vertical reflector is about 3 μs, elucidating a 59-μs difference between the two samples. The simulation result agrees well with the experimental one.

We also present the sound pressure profiles at various moments as a function of distance $d_{O(V)}$ in Figs. 3(c) and 3(g) for the oblique and vertical reflectors, respectively. At $t = 22$ μs, an ultrasound wave peak is observed at $d_{O(V)} = 17a$, and the

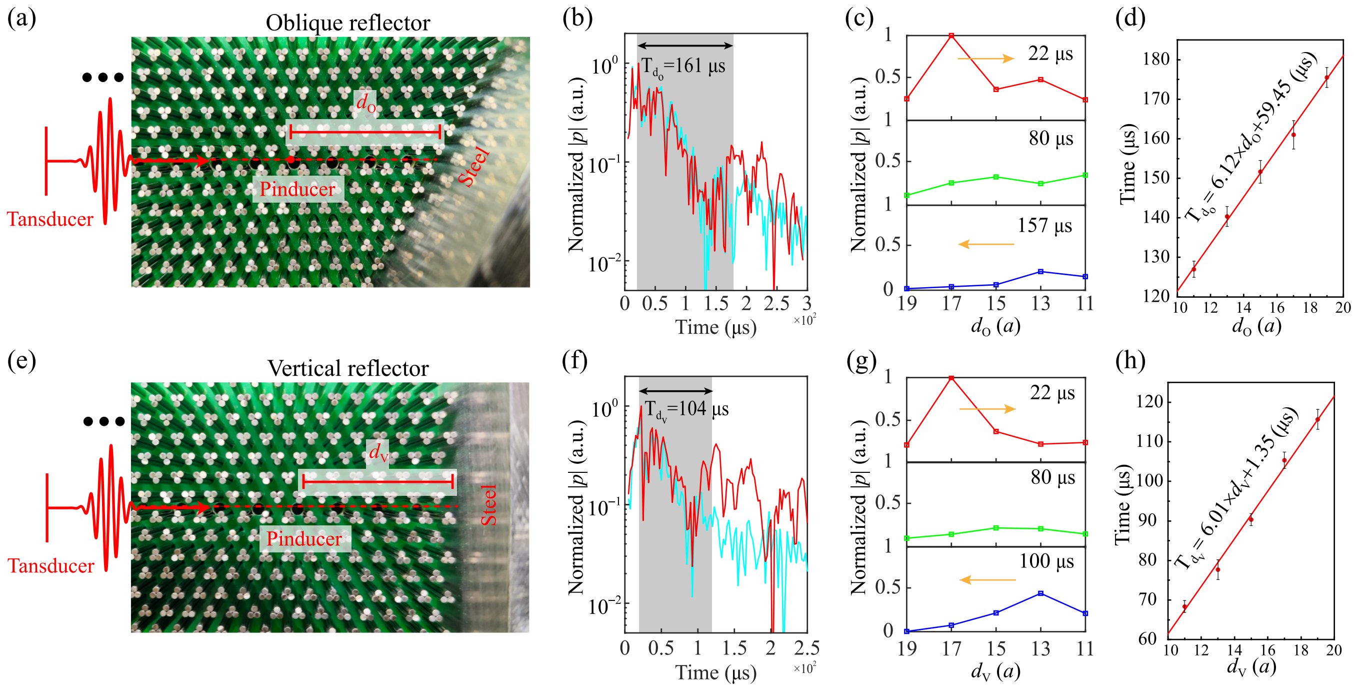

FIG. 3. (a) Photograph of the experimental sample featuring topological ultrasound cavities, terminated by the oblique steel reflector. The sound pulse is excited by a transducer positioned to the left of the sample. The dashed line outlines the waveguide interface, and the red dot indicates the probe position used by the pinducer. (b) Temporal variation of sound pressure inside the sample at the distance $d_O = 17a$. The shaded region highlights the time difference between the incident and reflected signals. The red and cyan lines represent the measured signals with and without the reflector, respectively. (c) Sound pressure distribution at three distinct times. Arrows indicate the propagation directions of the signal. (d) Measured time difference between incident and reflected signals at various positions d_V, with their linear fitting. (e–h) Same as (a)–(d), but for the topological cavities terminated by a vertical steel reflector.

ultrasound waves continue to propagate to the right along the VSC interfaces. At $t = 80$ μs, the waves arrive at the rigid reflector surface. For the oblique reflector, the reflected wave reaches $d_O = 13a$ at 157 μs, continuing to propagate to the left. For the vertical reflector, the reflected wave arrives at $d_V = 13a$ at 100 μs. This highlights a temporal difference of 57 μs between the two ultrasound cavities. The longer valley-flipping time in the oblique reflector sample allows for greater wave accumulation at the intersection, thereby forming a more localized cavity. Consequently, the reflected waves are weaker than those in the vertical reflector. We also plot the time difference between the incident and reflected waves along the waveguide as a function of distance $d_{O(V)}$ in Figs. 3(d) and 3(h) for the oblique and vertical reflector, respectively. The incident wave frequency is set to 0.3 MHz. The group velocity and valley-flipping time are extracted by fitting the data to the equation $T_{d_{O(V)}} = \frac{2d_{O(V)}}{V_g} + t_f$. From this, we obtain a group velocity of 0.61 c_w for the valley edge state. The valley-flipping times are found to be 59.45 μs for the oblique reflector and 1.35 μs for the vertical reflector, yielding a difference of 58.1 μs. This disparity in flipping time indicates a more substantial accumulation of ultrasound waves in the oblique reflector sample, leading to the formation of a high-quality factor topological ultrasound cavity. (The calculation of the quality factor for the samples and related impacts can be found in the Supplemental Material [50].) The acoustic wave accumulation is minimal in the vertical reflector, and the valley edge state is almost immediately reflected at the intersection.

We finally perform the study of the VSC waveguide terminated with a rigid reflector at angles ranging from 60° to 90°, to elucidate the formation mechanism of the topological cavity. The schematics for the configurations at angles 70° and 80° are presented in Figs. 4(a) and 4(d), respectively, with L denoting the distance between the center of meta-molecules and the reflector. As shown in Figs. 4(b) and 4(e), we calculate the eigenfields for both configurations across three different distances at a frequency of $f = 0.302$ MHz. There are no strong localized fields along the waveguide, signifying the absence of a topological ultrasonic cavity, which stands in stark contrast to the situation observed at an angle of 60° in Fig. 2(a). Furthermore, we calculate the eigenfields for both configurations at a distance of $L = 0.8a$ for three different frequencies, as illustrated in Figs. 4(c) and 4(f). The results again reveal a lack of strong localized fields along the waveguide. For the rigid reflector at random angles (70° or 80°), the oblique interface appears to disrupt the scattering of VSCs, suggesting a breakdown of local periodicity within the VSCs. This irregular local boundary can give rise to disordered states that further inhibit the formation of a topological ultrasonic cavity.

In summary, we have successfully demonstrated the realization of a geometry-dependent underwater topological ultrasound cavity using a VSC waveguide, terminated by

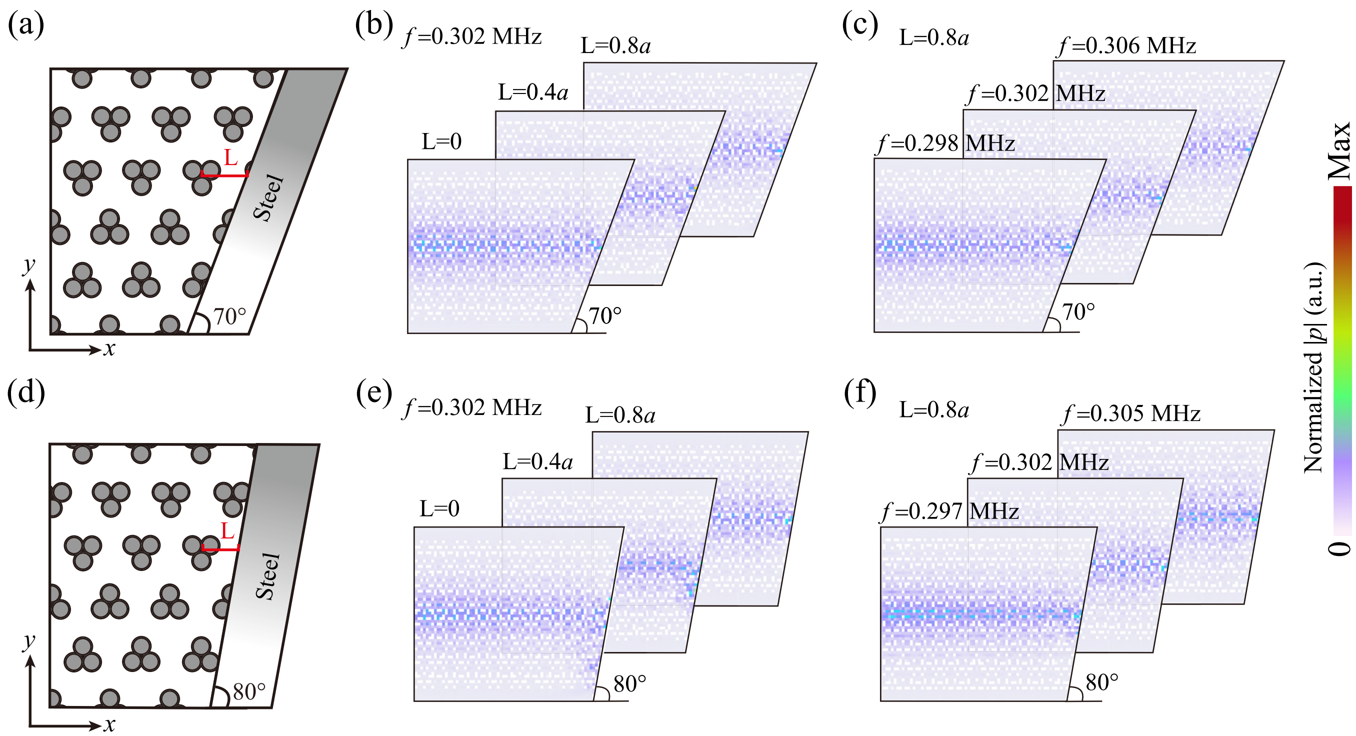

FIG. 4. (a) Schematic of a VSC waveguide terminated by a 70° oblique reflector. The distance between the center of meta-molecules and the reflector is denoted as L. (b) The eigenfields of the configurations under three distances $L = 0$, $0.4a$, and $0.8a$ at a frequency of $f = 0.302$ MHz. (c) The eigenfields of the configuration for distance $L = 0.8a$ at three different frequencies. (d)–(f) Same as (a)–(c), but for the configurations for the 80° reflector.

a rigid reflector. The design exploits the unique properties of VSCs to manipulate sound wave propagation, resulting in strong confinement of sound energy along the reflector surface. Through both frequency- and time-domain ultrasound measurements, we have experimentally confirmed the mechanism behind this confinement, which arises from the extended time delay associated with valley-polarized flipping as the waves interact with the reflector. The edge configuration of the VSCs, combined with the oblique angle of the reflector, significantly influences the valley-flipping duration, offering an effective means to fine-tune the performance of topological ultrasound cavities. Our findings contribute to the growing field of underwater topological acoustics, highlighting the potential for designing high-quality topological cavities with controlled acoustic wave dynamics, and also contribute to the underwater positioning applications [52].

This work is supported by the National Key R&D Program of China (Grant No. 2023YFB2804701) and the National Natural Science Foundation of China (Grants No. 12374419, No. 12522409, No. 12574024, No. 12574484, and No. U25D8001).

Data availability. The data that support the findings of this article are not publicly available because of legal restrictions preventing unrestricted public distribution. The data are available from the authors upon reasonable request.

[1] M. Z. Hasan and C. L. Kane, *Colloquium:* Topological insulators, Rev. Mod. Phys. **82**, 3045 (2010).
[2] X.-L. Qi and S.-C. Zhang, Topological insulators and superconductors, Rev. Mod. Phys. **83**, 1057 (2011).
[3] N. P. Armitage, E. J. Mele, and A. Vishwanath, Weyl and Dirac semimetals in three-dimensional solids, Rev. Mod. Phys. **90**, 015001 (2018).
[4] T. Ozawa, H. M. Price, A. Amo, N. Goldman, M. Hafezi, L. Lu, M. C. Rechtsman, D. Schuster, J. Simon, O. Zilberberg, and I. Carusotto, Topological photonics, Rev. Mod. Phys. **91**, 015006 (2019).
[5] G. Ma, M. Xiao, and C. T. Chan, Topological phases in acoustic and mechanical systems, Nat. Rev. Phys. **1**, 281 (2019).
[6] B. Q. Lv, T. Qian, and H. Ding, Experimental perspective on three-dimensional topological semimetals, Rev. Mod. Phys. **93**, 025002 (2021).
[7] H. Xue, Y. Yang, and B. Zhang, Topological acoustics, Nat. Rev. Mater. **7**, 974 (2022).
[8] W. Zhu, W. Deng, Y. Liu, J. Lu, H.-X. Wang, Z.-K. Lin, X. Huang, J.-H. Jiang, and Z. Liu, Topological phononic metamaterials, Rep. Prog. Phys. **86**, 106501 (2023).
[9] T. Shah, C. Brendel, V. Peano, and F. Marquardt, Colloquium: Topologically protected transport in engineered mechanical systems, Rev. Mod. Phys. **96**, 021002 (2024).
[10] Z. Zhang, H. Long, C. Liu, C. Shao, Y. Cheng, X. Liu, and J. Christensen, Deep-subwavelength holey acoustic

second-order topological insulators, Adv. Mater. **31**, 1904682 (2019).

[11] B. Ungureanu, M. P. Makwana, R. V. Craster, and S. Guenneau, Localizing elastic edge waves via the topological rainbow effect, Phys. Rev. Appl. **15**, 014057 (2021).

[12] C. Lu, C. Wang, M. Xiao, Z. Q. Zhang, and C. T. Chan, Topological rainbow concentrator based on synthetic dimension, Phys. Rev. Lett. **126**, 113902 (2021).

[13] C. Lu, Y.-Z. Sun, C. Wang, H. Zhang, W. Zhao, X. Hu, M. Xiao, W. Ding, Y.-C. Liu, and C. T. Chan, On-chip nanophotonic topological rainbow, Nat. Commun. **13**, 2586 (2022).

[14] A. Rycerz, J. Tworzydlo, and C. W. J.Beenakker, Valley filter and valley valve in graphene, Nat. Phys. **3**, 172 (2007).

[15] D. Xiao, W. Yao, and Q. Niu, Valley-contrasting physics in graphene: Magnetic moment and topological transport, Phys. Rev. Lett. **99**, 236809 (2007).

[16] K. F. Mak, K. L. McGill, J. Park, and P. L. McEuen, The valley Hall effect in MoS_2 transistors, Science **344**, 1489 (2014).

[17] J. Lu, C. Qiu, L. Ye, X. Fan, M. Ke, F. Zhang, and Z. Liu, Observation of topological valley transport of sound in sonic crystals, Nat. Phys. **13**, 369 (2017).

[18] J.-W. Dong, X.-D. Chen, H. Zhu, Y. Wang, and X. Zhang, Valley photonic crystals for control of spin and topology, Nat. Mater. **16**, 298 (2017).

[19] M. Yan, J. Lu, F. Li, W. Deng, X. Huang, J. Ma, and Z. Liu, On-chip valley topological materials for elastic wave manipulation, Nat. Mater. **17**, 993 (2018).

[20] Q. Zhang, D. Lee, L. Zheng, X. Ma, S. I. Meyer, L. He, H. Ye, Z. Gong, B. Zhen, K. Lai, and A. T. Charlie Johnson, Gigahertz topological valley Hall effect in nanoelectromechanical phononic crystals, Nat. Electron. **5**, 157 (2022).

[21] F. F. Li, H. X. Wang, Z. Xiong, Q. Lou, P. Chen, R. X. Wu, Y. Poo, J. H. Jiang, and S. John, Topological light-trapping on a dislocation, Nat. Commun. **9**, 2462 (2018).

[22] J. Noh, W. A. Benalcazar, S. Huang, M. J. Collins, K. P. Chen, T. L. Hughes, and M. C. Rechtsman, Topological protection of photonic mid-gap defect modes, Nat. Photon. **12**, 408 (2018).

[23] X. Gao, L. Yang, H. Lin, L. Zhang, J. Li, F. Bo, Z. Wang, and L. Lu, Dirac-vortex topological cavities, Nat. Nanotechnol. **15**, 1012 (2020).

[24] Z. K. Shao, H. Z. Chen, S. Wang, X. R. Mao, Z. Q. Yang, S. L. Wang, X. X. Wang, X. Hu, and R. M. Ma, A high-performance topological bulk laser based on band-inversion-induced reflection, Nat. Nanotechnol. **15**, 67 (2020).

[25] Y. Liu, S. Leung, F. F. Li, Z. K. Lin, X. Tao, Y. Poo, and J.-H. Jiang, Bulk–disclination correspondence in topological crystalline insulators, Nature (London) **589**, 381 (2021).

[26] Z. K. Lin, Q. Wang, Y. Liu, H. Xue, B. Zhang, Y. Chong, and J.-H. Jiang, Topological phenomena at defects in acoustic, photonic and solid-state lattices, Nat. Rev. Phys. **5**, 483 (2023).

[27] Y. Deng, W. A. Benalcazar, Z.-G. Chen, M. Oudich, G. Ma, and Y. Jing, Observation of degenerate zero-energy topological states at disclinations in an acoustic lattice, Phys. Rev. Lett. **128**, 174301 (2022).

[28] Y. Chen, Y. Yin, Z.-K. Lin, Z.-H. Zheng, Y. Liu, J. Li, J.-H. Jiang, and H. Chen, Observation of topological p-orbital disclination states in non-Euclidean acoustic metamaterials, Phys. Rev. Lett. **129**, 154301 (2022).

[29] J. Wu, Y. Hu, Z. He, K. Deng, X. Huang, M. Ke, W. Deng, J. Lu, and Z. Liu, Hybrid-order skin effect from loss-induced nonreciprocity, Phys. Rev. Lett. **134**, 176601 (2025).

[30] M. A. Bandres, S. Wittek, G. Harari, M. Parto, J. Ren, M. Segev, D. N. Christodoulides, and M. Khajavikhan, Topological insulator laser: Experiments, Science **359**, eaar4005 (2018).

[31] G. Harari, M. A. Bandres, Y. Lumer, M. C. Rechtsman, Y. D. Chong, M. Khajavikhan, D. N. Christodoulides, and M. Segev, Topological insulator laser: Theory, Science **359**, eaar4003 (2018).

[32] Y. Zeng, U. Chattopadhyay, B. Zhu, B. Qiang, J. Li, Y. Jin, L. Li, A. G. Davies, E. H. Linfield, B. Zhang, Y. Chong, and Q. J. Wang, Electrically pumped topological laser with valley edge modes, Nature (London) **578**, 246 (2020).

[33] L. Yang, G. Li, X. Gao, and L. Lu, Topological-cavity surface-emitting laser, Nat. Photon. **16**, 279 (2022).

[34] Y. Yang, Y. Yamagami, X. Yu, P. Pitchappa, J. Webber, B. Zhang, M. Fujita, T. Nagatsuma, and R. Singh, Terahertz topological photonics for on-chip communication, Nat. Photon. **14**, 446 (2020).

[35] W. Wang, Y. J. Tan, T. C. W. Tan, A. Kumar, P. Pitchappa, P. Szriftgiser, G. Ducournau, and R. Singh, On-chip topological beamformer for multi-link terahertz 6G to XG wireless, Nature (London) **632**, 522 (2024).

[36] M. Hafezi, E. A. Demler, M. D. Lukin, and J. M. Taylor, Robust optical delay lines with topological protection, Nat. Phys. **7**, 907 (2011).

[37] Z. Zhang, Y. Tian, Y. Cheng, Q. Wei, X. Liu, and J. Christensen, Topological acoustic delay line, Phys. Rev. Appl. **9**, 034032 (2018).

[38] S. Barik, A. Karasahin, C. Flower, T. Cai, H. Miyake, W. DeGottardi, M. Hafezi, and E. Waks, A topological quantum optics interface, Science **359**, 666 (2018).

[39] Y. Li, Y. Yu, F. Liu, B. Zhang, and G. Shvets, Topology-controlled photonic cavity based on the near-conservation of the valley degree of freedom, Phys. Rev. Lett. **125**, 213902 (2020).

[40] B. Yan, B. Liao, F. Shi, X. Xi, Y. Cao, K. Xiang, Y. Meng, L. Yang, Z. Zhu, J. Chen, X.-D. Chen, G.-G. Liu, B. Zhang, and Z. Gao, Realization of topology-controlled photonic cavities in a valley photonic crystal, Phys. Rev. Lett. **134**, 033803 (2025).

[41] J. Lu, C. Qiu, M. Ke, and Z. Liu, Valley vortex states in sonic crystals, Phys. Rev. Lett. **116**, 093901 (2016).

[42] L. Ye, C. Qiu, J. Lu, X. Wen, Y. Shen, M. Ke, F. Zhang, and Z. Liu, Observation of acoustic valley vortex states and valley-chirality locked beam splitting, Phys. Rev. B **95**, 174106 (2017).

[43] J. Lu, C. Qiu, W. Deng, X. Huang, F. Li, F. Zhang, S. Chen, and Z. Liu, Valley topological phases in bilayer sonic crystals, Phys. Rev. Lett. **120**, 116802 (2018).

[44] M. Wang, Q. Ma, S. Liu, R. Y. Zhang, L. Zhang, M. Ke, Z. Liu, and C. T. Chan, Observation of boundary induced chiral anomaly bulk states and their transport properties, Nat. Commun. **13**, 5916 (2022).

[45] Z. D. Zhang, M. H. Lu, and Y. F. Chen, Observation of free-boundary-induced chiral anomaly bulk states in elastic twisted kagome metamaterials, Phys. Rev. Lett. **132**, 086302 (2024).

[46] H. Wu, H. He, L. Ye, J. Lu, M. Ke, W. Deng, and Z. Liu, Acoustic valley filter, valve, and diverter, Adv. Mater. **37**, 2500757 (2025).

[47] E. Dong, P. Cao, J. Zhang, S. Zhang, N. Fang, and Y. Zhang, Underwater acoustic metamaterials, Natl. Sci. Rev. **10**, nwac246 (2023).

[48] Y. Shen, C. Qiu, X. Cai, L. Ye, J. Lu, M. Ke, and Z. Liu, Valley-projected edge modes observed in underwater sonic crystals, Appl. Phys. Lett. **114**, 023501(2019).

[49] F. Li, F. Cai, L. Zhang, Z. Liu, F. Li, L. Meng, J. Wu, J. Li, X. Zhang, and H. Zheng, Phononic-crystal-enabled dynamic manipulation of microparticles and cells in an acoustofluidic channel, Phys. Rev. Appl. **13**, 044077 (2020).

[50] See Supplemental Material at http://link.aps.org/supplemental/10.1103/hf4m-sql4 for more details of (I) the comparative analysis of valley-flipping characteristics in oblique reflector and vertical reflector acoustic cavities; (II) eigenfields of the waveguide mode with the presence of a rigid reflector; (III) the calculation of the Q factor of the topological ultrasound cavity; (IV) simulation results of the topological ultrasound cavity; (V) the time difference for different $d_{\mathrm{O(V)}}$ values (simulations and experiments); (VI) the method to extract the delay time between the incident and reflected packet in experiments; (VII) the topological ultrasonic cavity at different frequencies; and (VIII) the topological ultrasonic cavity for different pulse widths, which also contains Refs. [39,40].

[51] F. Gao, H. Xue, Z. Yang, K. Lai, Y. Yu, X. Lin, Y. Chong, G. Shvets, and B. Zhang, Topologically protected refraction of robust kink states in valley photonic crystals, Nat. Phys. **14**, 140 (2018).

[52] S. Zheng, G. Duan, and B. Xia, Underwater acoustic positioning based on valley-chirality locked beam of sonic system, Int. J. Mech. Sci. **174**, 105463 (2020).